Complete neuroanatomy and sensor maps of dragonfly wings for fly-by-feel monitoring of aeroelasticity

Joseph Fabian[1,2]*, Igor Siwanowicz[3]*, Myriam Uhrhan[1], Masateru Maeda[4], Richard J Bomphrey[4] and Huai-Ti Lin[1]**

1. Imperial College London
2. Flinders University
3. HHMI Janelia Research Campus
4. Royal Veterinary College

*equal contribution authors
** corresponding author

Summary

'Fly-by-feel' describes how mechanosensory systems capture aerodynamic and inertial information to enable or enhance flight control. Most studies on animal flight emphasized body stabilization via visual or inertial sensory inputs and it has been demonstrated that wing sensory systems can provide inertial state estimation for the body. Can wing mechanosensors provide extensive reconstruction of the wing aeroelastic states? Little is known about how flying animals utilize their wing sensory systems to monitor the dynamic state of their highly deformable wings. Odonata, dragonflies and damselflies, is a basal lineage of flying insects with excellent flight performance, and their wing mechanics have been studied extensively. Here, we present a complete map of the wing sensory system for two Odonata species, including both the external sensor morphologies and internal neuroanatomy. We identified eight morphological classes of sensors, most of which were innervated by a single neuron and resembled mechanosensors. Their innervation patterns are consistent with minimising wiring length. We further mapped the major veins of another 13 Odonata species across 10 families and identified consistent sensor distribution patterns, with sensor count scaling with wing length. To explore how strain sensing could contribute to the wing state estimation, we constructed a high-fidelity finite element model of a dragonfly wing based on micro-CT imaging. Our dynamic, flapping wing model revealed features of the strain fields and suggested how increasing sensor count could allow encoding of different wing states. Taken together, this work moves toward an integrated understanding of fly-by-feel control in animal flight.

Introduction

Animal locomotion relies on sensory feedback to implement reflexes [1,2], plan future events [3,4] and accumulate experiences for motor learning [5]. In terrestrial animals, proprioceptors in joints and muscles establish the timing and magnitude of important mechanical events during walking. The wings of flying animals experience a combined inertial-aerodynamic ('aeroelastic') loads, airflow stagnation and separation, and non-linear phenomena of vortex growth and shedding, generated during gliding and flapping flight [6–8]. The current literature on mechanical feedback during flight consists of isolated reports of specific sensor types, often accompanied by proposals of their functional significance for flight control. The feather follicles of birds possess mechanosensors sensitive to feather motion under aeroelastic forces [9,10], while the wings of bats and moths are populated with mechanosensors which are known to contribute to flight control and body stabilisation [11,12]. However, complete descriptions of the sensor arrangement on the wings of a flying animal have been elusive. Animal wings express a diverse array of mechanosensors each capturing specific and localised information. As with sensory receptors in other organs, such as the eye, it is likely that arrays of receptors function in concert, each contributing a piece to a larger, time-dependent, sensory mosaic [13,14]. Therefore, to understand the function of sensory feedback during flight we must first determine a comprehensive map of mechanosensors on wings.

While fly-by-feel may be implemented differently in different flying animals, insects are a useful model for their relatively simple nervous system and the absence of actuation beyond the wing base. These features make comprehensive sensor mapping and mechanical analyses tractable. Flapping flight relies on the phasic generation of precise aerodynamic forces through coordinating wing movements. Dragonflies are especially interesting due to their four independently controlled wings, each with adjustable amplitude, frequency, and angle of attack [15,16]. This enables a large wing state-space, each with unique, and time-dependent, aerodynamic and inertial characteristics. Dragonflies can fly by synchronised flapping of all four wings, out-of-phase flapping of forewing and hindwing, isolated flapping of the forewings only, gliding with the wings in a more-or-less fixed positions, and even in mechanically linked tandem flights with a mating partner. From a practical perspective, dragonfly wings have exposed wing veins with transparent, scaleless membranes, which facilitate the characterization of external and internal anatomy.

The concept of sensory feedback from insect wings has received attention from neuroscientists and engineers since the 1960's, following the discovery of neurons sensitive to wing twist in locusts [17,18]. Further electrophysiological studies described the afferent signals of campaniform sensilla in the wings of flies [19]. The sensory neurons attached to these strain sensors tend to fire a single action potential per wing stroke, so they cannot provide continuous strain estimation. Instead, strain is believed to be encoded predominantly through spike timing, which varies with the neurons strain threshold, and the temporal dynamics of local strain [12,20]. Unlike other insects, flies have specialized club-like structures called halteres, derived from their reduced hindwings. Instead of producing aerodynamic forces during flight, the halteres express strain sensors which allow estimation of the insect's body rotation through the detection of the Coriolis forces [21]. All flapping insect wings experience similar Coriolis forces, and recent work has demonstrated that strain sensor arrays on wings also function as inertial sensors, much like the halteres [22–24] . In fact, to detect body rotation through a flapping wing, only relatively few sparsely distributed strain sensors are needed [25]. This is consistent with the sparse distribution of campaniform sensilla found in some insects [26]. However, the wing-mounted sensors are well-placed to monitor the instantaneous aeroelastic loading conditions and flow velocities of the wings themselves. This line of investigation is far less developed and can impact our understanding of flight control in flying insects, flying vertebrates and also inspire novel flight controllers in an engineering context.

Here we provide the most complete description of the mechanosensory system of an animal wing to date. Specifically, we identify the patterns of neural innervation and the locations of all sensor types found in Odonata. Integrating this comprehensive map with a high-fidelity finite element model of a flapping dragonfly wing, we demonstrate how strain sensing can contribute to the state estimation of a highly deformable wing.

Results and Discussion

Odonata wing veins house an extensive network of sensory neurons

To visualise the neuronal innervation within Odonata wings, we developed a new approach for labelling and imaging the complete collection of wing neurons and associated cuticular structures (see Methods). For comparison, we visualised wings from a small dragonfly species *Perithemis tenera* and a similarly sized damselfly *Argia apicalis*. We identified axons of sensory neurons in all major longitudinal veins. Some of these axons run the entire wing length, making them among the longest neurons in the dragonfly. Axons terminate with a soma which is almost always located directly under an external cuticular structure. Each neuron follows a direct path from the wing hinge to its soma (Figure 1A,B), with some minor variation between individuals (Figure S1C,D). Unlike the leading edge and the longitudinal veins, the trailing edge of dragonfly wings has no dedicated axon tract. Instead, it is innervated locally by extensions of the closest longitudinal vein tracts. This could reduce total axon length, since the medial region of the trailing edge follows a curved and less direct path compared to other major veins. This arrangement will also minimize the impact of typical wing damage, which is almost exclusively found on the

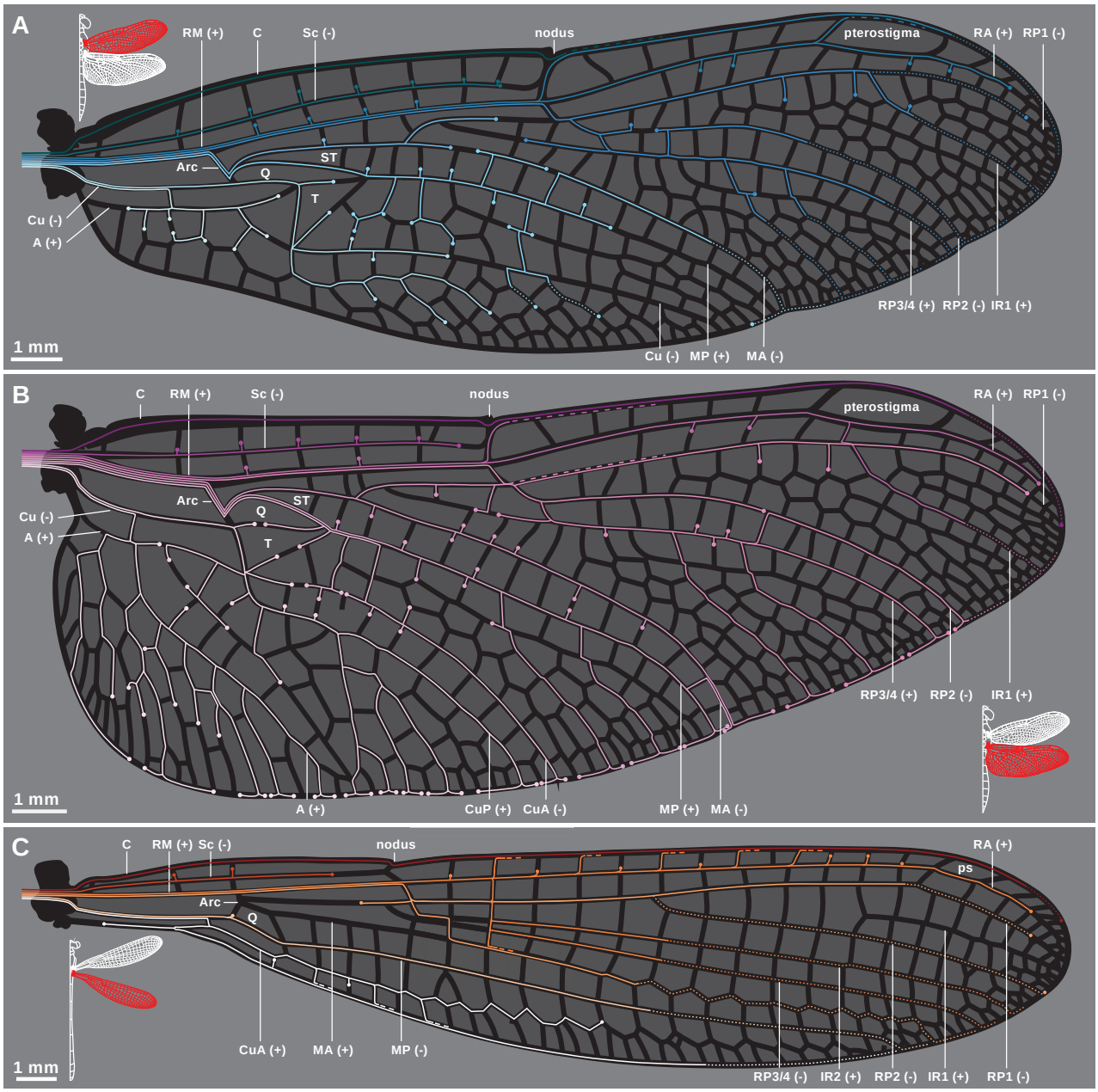

Figure 1. The axon routing pattern of selected Odonates. Neuronal innervation diagram of male Eastern Amberwing dragonfly (*Perithemis tenera*) forwing **(A)**, hindwing **(B)** and a male Blue Fronted Dancer damselfly (*Argia apicalis*) hindwing **(C)**. A dedicated afference wing nerve branches out into different veins from the wing base. The color tones of axonal tracks were chosen arbitrarily for readability. They do not imply hierarchy or relationship of the tracks. Dots indicate the ends of axonal track; dashed lines denote merging tracks; dotted lines represent tracks that were interpolated from incomplete back-fill images and mechanosensors found on the veins. Major veins and structural elements of the wings are labeled following the system of [75] and [76]: C- costa; Sc - subcosta; RM - radius/media; Cu - cubitus; A - anal; Arc - arculus; T - triangle; ST - supratriangle; Q - quadrilateral. The corrugations of the wings/ topology of veins are represented by "+" for "ridges" (dorsally convex) and "-" for "valleys" (dorsally concave).

trailing edges for dragonflies [27]. If trailing edge sensory neurons were routed along the trailing edge vein, even a small local break could eliminate the function of all sensors distal to the damage.

In contrast to the *P. tenera* (dragonfly), the venation pattern of *A. apicalis* (damselfly) wings consists of mostly well aligned rectangular cells, resembling an aerial view of a modern city grid. The innervation pattern of the damselfly wing is similar to that of the dragonfly, with some exceptions (Figure 1C). Unlike the dragonfly wing, the trailing edge of the damselfly wing is innervated directly, with a tract of axons running along the length of the trailing edge. Due to the wing shape, axons can pass through the damselfly trailing edge without any detour cost. Furthermore, the natural wing wear for wild damselflies are typically not at the trailing edge thus the risk of sensory loss is less. All wing neurons can be traced back to the meso- and meta-thoracic ganglia via anterior and posterior wing nerves passing through the wing base. These two nerves converge before merging into the most anterior nerve bifurcation of each ganglion [28,29]. There is no evidence of synaptic connections between neurons within the wing, and the cell body counts exceed 750 and 350 (see later sections for exact counts) for each dragonfly and damselfly wing we mapped respectively. Together it suggests a significant influx of raw sensory signals traveling from the wing to the ganglia. The diversity and distribution of these wing sensors will be the focus of the following sections.

Wing sensor morphologies

Dragonfly wings are extensively innervated by sensory neurons, but what external cuticular structures are these neurons innervating? Odonata wing membranes are relatively smooth, but their veins are covered in an array of microscopic structures with a variety of roles [30,31]. Some microstructures resemble sensors but are not innervated. Using confocal microscopy imaging of a whole-mount wing, we traced individual axons branching from the primary bundle near the wing hinge to their cell bodies. These cell bodies send stubby dendrites towards the cuticular surface. Autofluorescence of this cuticular surface highlights a variety of structures. Based on our current understanding of insect wing sensors, we classified the wing sensory structures into eight classes: wing margin bristle-bump complexes (Figure 2A,B,C); bristle-bump complexes (Figure 2D); isolated bristles of varying length (Figure 2E,F); campaniform sensilla with associated structures (Figure 2G,H,J); isolated campaniform sensilla (Figure 2I,K,L); campaniform sensilla fields (Figure 2M,N); hair plates (Figure 2N,O); and multipolar cells (Figure 2P,Q,R).

The costa vein (leading edge) and trailing edge of the wing are covered in densely populated sensory bristles (~30 µm long), associated with teeth forming dorsal and ventral serrations (Figure 2A–C). Similar bristles have been found on the wing margin of moths, sensitive to directional vibratory airflow [32], and in drosophila, where manual stimulation triggers a defensive leg kicking response [33]. In the dragonfly, each bristle attaches to the dendrite of a sensory neuron at its base, and in up to 25% of cases a second sensory neuron sends its dendrite through the shaft of the bristle to its tip. These are the only external wing sensors that are innervated by more than one neuron, and we observed no pattern on their occurrence. We suspect double innervated bristles might serve as a chemosensor as seen in flies [34] as well as a mechanosensor. Dragonflies are often considered anosmic due to their minuscule antennal lobes [35], but there is some behavioural evidence suggesting odours are used to choose predation sites [36]. Dragonflies are not able to groom their wings like a fly and the wings do not come into contact due to folding, but we do not exclude the potential tactile functions for wing margin bristles. Other longitudinal veins have isolated bristles with lengths ranging from 20 µm (Figure 2E) to more than 200 µm (Figure 2F), each innervated by a single sensory neuron at their base. The longer bristles have wider base (3.3-3.4 µm). They resemble the trichoid sensilla found in locusts that detect wind direction and elicit compensatory reflexes [37–40].

The thickest longitudinal veins (subcosta, radius, cubitus, media) contain short (10–15 µm) bristles, each paired with small saw-tooth shaped bump (Figure 2D). The shape of these paired bumps is highly constant across the wing, and across multiple species, as is the spatial relationship between the bump and bristle. Each bristle lies several micrometres distal from the bump, which protrudes from the vein at a shallow gradient on its medial side,

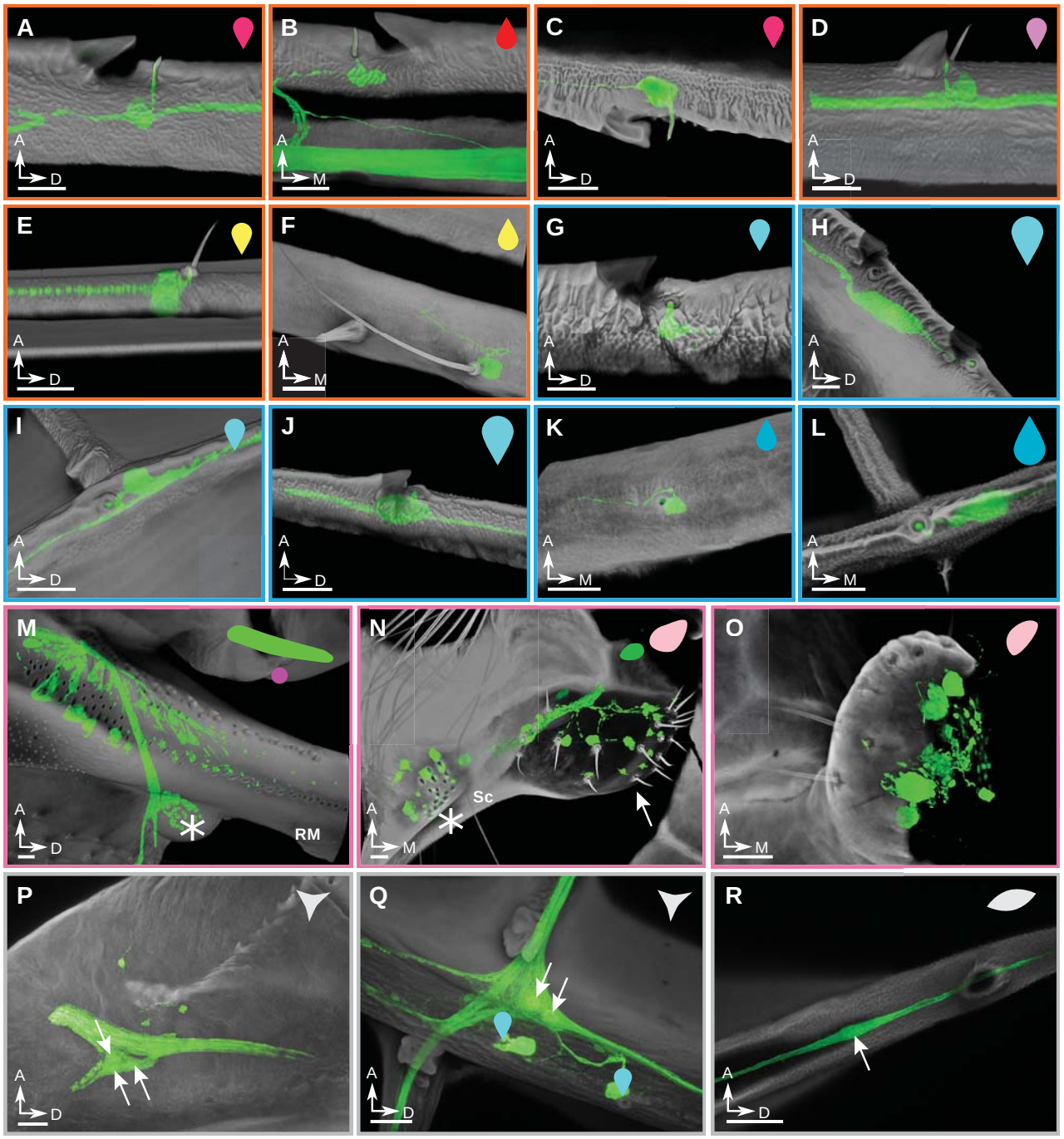

Figure 2. The classification and morphology of all wing sensors. Examples of sensors found on the wings of the dragonfly *Perithemis tenera*. The scale bars are all 25 µm. **(A-F)**: candidate airflow sensors; **(A)** dorsal costa margin bristle-bump; **(B)** ventral costa margin bristle-bump; **(C)** trailing edge margin bristle-bumps. All three examples show the double-innervated type of a bristle which consist only 25% of all the wing margin bristles. All other bristles have only one dendrite innervating the bristle base (not shown). **(D)** radius bristle-bump; all bristles of this type are innervated by one neuron at the base. **(E)** long bristle of the type present on the medial part of several major veins. **(F)** short bristle. **(G-L)**: strain sensors; **(G)** dorsal costa campaniform sensillum (CS); **(H)** large dorsal costa CS; **(I)** dorsal cross vein CS; **(J)** large radius anterior CS immediately distal to pterostigma; **(K)** ventral subcosta CS; **(L)** terminal ventral CS of the radius posterior 1 (RP1) vein. **(M-O)**: wing base sensory fields; **(M)** – crevice organ – two parallel fields of directionally tuned elliptical CS at the base of radius/media (RM) vein. Asterisk marks the dorsal insertion site of a wing base chordotonal organ; **(N)** hair plate (arrow) and two adjacent CS fields (asterisk) ventrally at the base of subcosta; **(O)** hair plate ventrally at the base of cubitus. **(P-R)**: multipolar and bipolar receptors: **(P)** multipolar receptor at the base of costa; arrows point to/indicate cell bodies; **(Q)** multipolar receptor located at the junction of the anal vein and the first/medial cross vein connecting it to cubitus. Two adjacent dorsal CS are indicated with cyan markers. **(R)** A bipolar receptor. All example images are from the right forewing, with cuticular autofluorescence in grey, and neurons labelled with Neurobiotin/Dyelight-584-Neutravidin in green. The symbols in the upper right corner of each panel are notations to show sensor type and dorsal/ventral placement which will be used in Fig 3.

and a steep gradient on its distal side. The bump itself is not innervated by a sensory neuron, and thus plays no direct sensory role. However, it has a conditioning effect on the external flow stimulus acting on the bristle, contributing to the tuning properties of the sensor (unpublished data). The bump might also play a protective role for the small bristles, functioning like a roll cage, preventing collisions or parasites from damaging the sensor arrays. To our knowledge, this bristle-bump sensory complex is novel and has not been described in any other animal.

A variety of strain sensitive campaniform sensilla are found on the costa (Figure 2G,H), and several other longitudinal veins (Figure 2I–L), often paired with the same type of saw-toothed cuticular bumps described for short bristles. On many of the joints connecting the radius longitudinal vein to cross veins, we observe isolated campaniform sensilla (Figure 2L), and at the base of the radius we see five fields of campaniform sensilla, each with an associated sensory neuron (Figure 2M). These sensor fields on the radius vein match the crevice organs described by Simmons [41], sensors whose name at the time reflects their resemblance of small pits on the cuticle. Fields of campaniforms with high aspect ratio pits are associated with directional strain sensing [42–44]. Specifically, two such fields on the subcostal have almost orthogonal directional bias which are conserved across odonates. In dipteran flies campaniform sensilla are found on both the wings and the halteres [45], and the ones on the halteres resemble the campaniform fields we observed. We also identify several hair plates on the wing base (Figure 2N,O), as well as a chordotonal organ, identified by its characteristic anatomy [46,47](Figure 2M). These sensory structures are typically associated with proprioception in insects [48,49]. Finally, we observe multiple multipolar neurons located at some joints between wing veins (Figure 2Q,R) with unknown function and no obvious associated cuticular structure.

A complete sensor map of Odonata wings

Aeroelastic loading of the wing during flight causes complex deformation of the architecture [50–52]. The flow patterns which have been observed on the wings of dragonflies during flight are similarly complex [16,53–59]. We expect the local placement and overall density of wing sensors is critical for capturing relevant information. Mechanosensors on the wing therefore directly inform control strategies either in real-time or by providing a training signal for fine-tuning a flight controller. Our imaging data allowed us to construct a complete sensory map of the dragonfly wing (Figure 3) in order to generate hypotheses of how a fly-by-feel controller might receive salient information.

Excluding the wing-base campaniform fields, we found a total of 771 on the forewing and 894 sensors on the hindwing of a dragonfly (*Perithemis tenera*), and 358 sensors on the hindwing of a damselfly (*Argia apicalis*). Extrapolating from this, we estimate this small dragonfly has well over 3000 wing sensors on its four wings, and the damselfly approximately half as many. Direct comparisons between sensor counts of other insects in the literature is difficult because current reports are incomplete, focusing on specific sensor types. Even though this is a very small species of dragonfly, the counts of equivalent sensor classes are significantly higher than those reported on the wings of moths, flies or beetles described so far [12,45,60]. One reason that might explain the great variation in wing sensory innervation across insects is the cost of maintaining the sensory neurons at the wing tips. Flying insects have a dedicated pump which circulates hemolymph through their wings, often all the way to the wing tip, to support neurons inside these veins [61–63]. This circulation likely involves considerable metabolic costs and, once established, the relative cost of additional sensors might be less significant. For these reasons we believe the cost-to-benefit relationship underlying sensor counts is likely non-linear, and a relatively dense sensor arrangement might be beneficial for some wings. Indeed, the dorsal side of the grasshopper wings show sensor counts comparable to those of the dragonfly [64]. Similarly, large number of sensory bristles have been found on locust hindwings [65].

Several patterns emerged from our complete Odonata wing maps. First, sensor types are clearly associated with local wing morphology, especially corrugation; for example, long trichoid sensilla are almost exclusively found in the wing's local valleys, while short bristles and bristle-bumps lie on local ridges. This arrangement could be

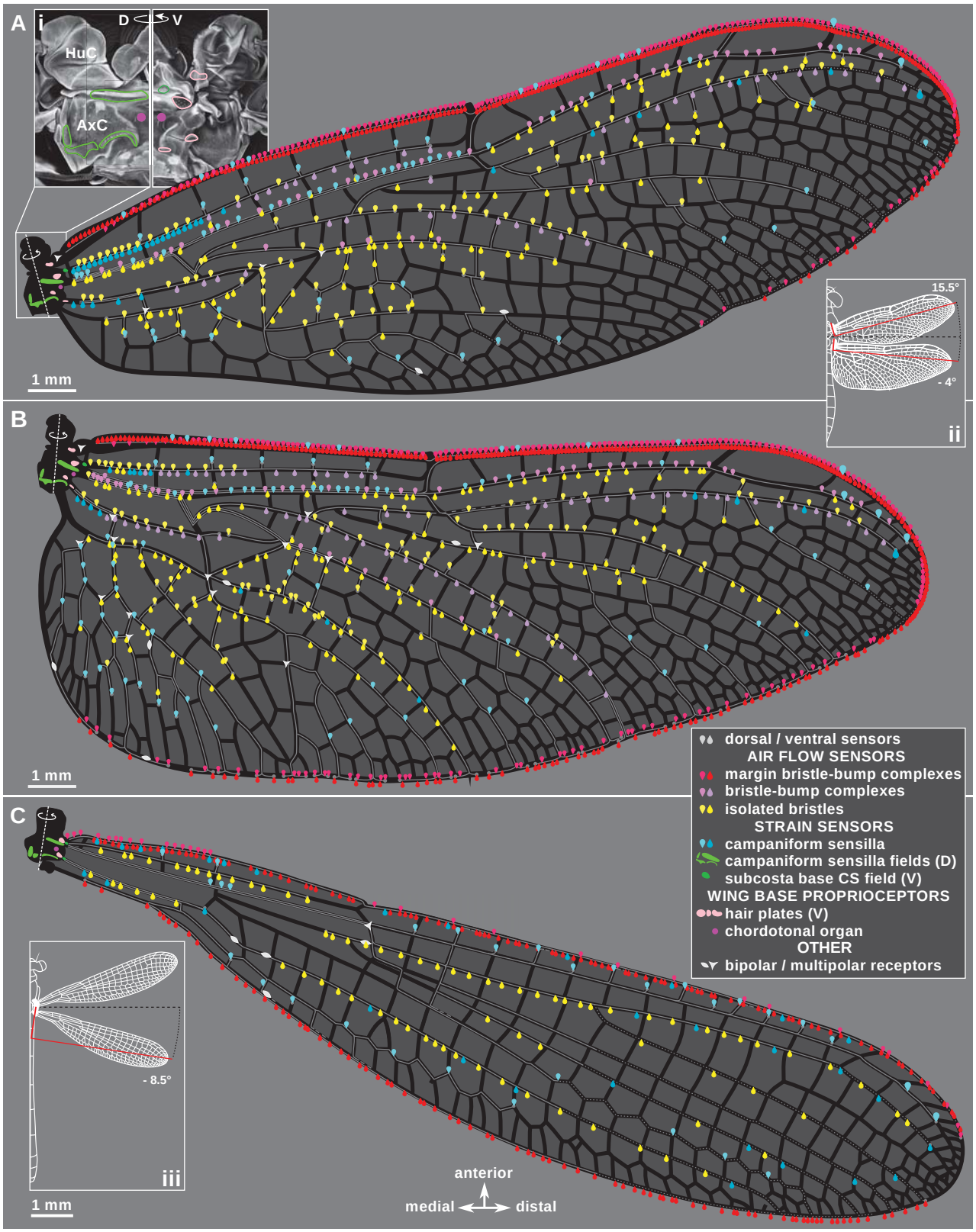

Figure 3. A sensory map of Odonate wings. Distribufion of all contirmed sensors on the *Perithemis tenera* dragonfly fore- **(A)** and hind **(B)** wings and a hindwing of *Argia apicalis* damselfly **(C)**. All sensor notafions follow Fig 2 and the tigure legend. Inset **(i)**: maximum intensity projecfion showing P. tenera right forewing base dorsally and ventrally with the sensor tields outlined. Insets **(ii)** and (**iii)**: diagrams showing the wings' natural sweep angles; the red reference lines mark the wing span axis perpendicular to the anatomical wing hinges.

suitable to detect the small eddies found within the corrugations as well as the attachment state of airflow [54]. Bristles without any bump dominate the central part of the wing blade in both the dragonfly and the damselfly. The length of these bristles varies ten-fold with bristle length decreasing from the wing base to the wing tip. Since the air speed increases from wing root to wing tip during flapping flight, the boundary layer thickness may reduce toward the wing tip. Therefore, the reduction of sensory bristle length may be consistent with the reducing boundary layer height toward the wing tip during flapping flight. However, the actual flow field around flapping wings is highly unsteady and may only intermittently follow this pattern. We suggest a more detailed aerodynamic study considering the distribution and morphology of the bristles is necessary to confirm this idea.

Second, the isolated campaniform sensilla are sparsely distributed around the edge of the wing. This ring-like arrangement is consistent with capturing the twist of the wing blade efficiently, as the largest deformations occur at a distance from the axis of twist [66,67]. Sporadic campaniform sensilla are found along the costa, yet the most posterior campaniform sensilla are located some distance away from the actual trailing edge. This margin may prevent sensor damage from wing wear, and avoid noisy trailing edge aeroelastic flutters. We found a total of 84 and 98 isolated campaniform sensilla on fore and hindwing of *Perithemis tenera*, respectively, with a bias towards the dorsal surface. The abundance of each sensor type varies considerably, bristles significantly outweigh campaniform sensilla on most veins. Interestingly, the damselfly wings studied are completely devoid of bristle-bump complexes or dorsal bristles (Figure 3C). This could be a result of the shallower corrugation.

Third, both the leading and trailing edges are densely populated with sensory bristles. These are by far the most abundant, accounting for approximately 60% of all wing sensors. Dragonflies generate a strong leading-edge vortex which is shed during the wing stroke cycle [16,54]. Consequently, the wing edges in flapping flight tend to experience large fluctuating pressure gradients [59] and experience cyclic changes of airflow direction. The bristles on the wing margin may, therefore, play a key role in detecting the timing and intensity of vortex formation and shedding. Similar sensors exist in moths and are known to be sensitive to directional vibratory airflow [68]. In the dragonfly, these sensory bristles are absent in the proximal 2/3rds of the forewing trailing edge. This area of absence matches the area of hindwing overlap during a flapping cycle. This pattern has been observed in the wing margin bristles of a butterfly's forewing and hindwing [69], suggesting a possible common strategy to avoid unwanted signals from wing collisions.

Fourth, in general wing sensors are placed with increasing sparsity from anterior to posterior, and from medial to distal. Each sensor has a cost in terms of mass, moment of inertia, metabolic energy, and increased complexity for decoding. For this reason, we expect biological sensor arrays will use the most sparse sensor arrangements that provide sufficient performance with adequate robustness. Simulations of sparse strain sensor systems show that performance is strongly dependent on sensor placement, with optimised sensor arrays resulting in significant reduction in the required number of sensors [66]. Mechanical stress on flapping wings is largest close to the wing base, and the metabolic cost of neuronal signalling increases in proportion to the length of an axon, therefore a bias towards medial sensor placement is likely to increase the efficiency of the sensory system.

Finally, the radius and axillary complex at the wing base are adorned with five fields of campaniform sensilla with 30–90 sensors per cluster (Figure 3A, inset). Both structures are load bearing, transmitting forces from thoracic muscles to the wings and flight forces from the wings to the body. Their sensilla have high aspect ratios, indicating high directional selectivity. Sensor orientations vary within each field, which might reflect the pattern in the wing base loading during both flapping and gliding flight and mechanical filtering. Their functions can range from inertial sensing to wing loading monitoring. There are a handful of multipolar cells scattered at specific cross-vein locations with no associated external structures and, as such, we do not include them for discussion here. Their function remains to be clarified.

A comparison of sensor distribution across Odonata families

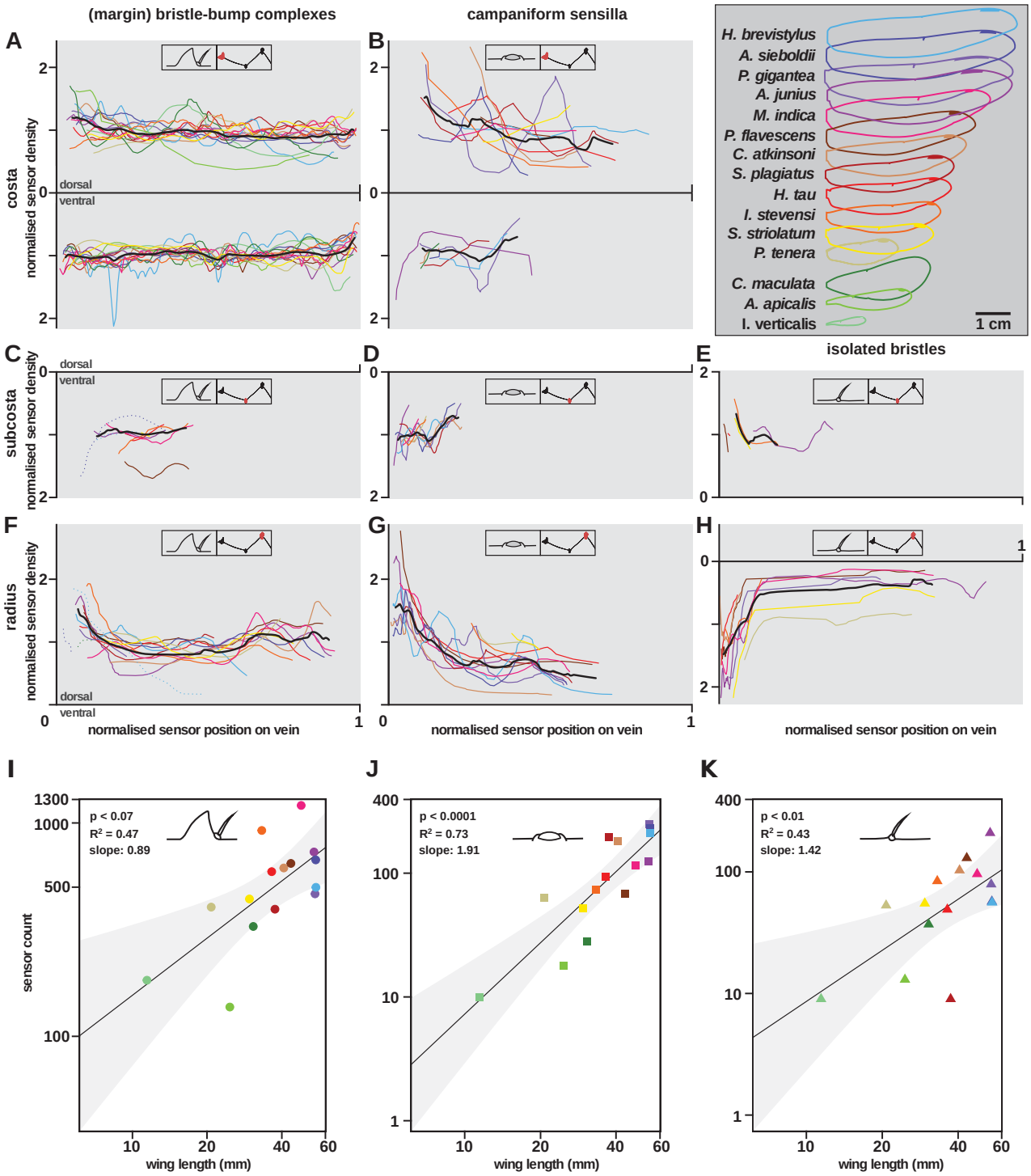

Figure 4. A comparison of sensor distribution across dragonfly families. Sensor density distribution **(A-H)** and sensor count **(I-K)** of the wing sensor types (bristle-bump complexes, campaniform sensilla and isolated bristles) across 15 Odonate species. Normalised sensor density is shown for dorsal and ventral side over normalised sensor position on three longitudinal veins, costa **(A-B)**, subcosta **(C-E)** and radius **(F-H)**. The insets in each panel highlight sensor type and the respective vein. Sensor density is normalized by the mean of each density curve. Sensor position is normalised by the length of the respective right forewing. The black bold line shows the mean of all species in each plot. **(I-K)** Sensor count is the sum for each sensor type of all three longitudinal veins. The sensor count is plotted over the respective wing length for each species. Black line shows the ordinary least squares (OLS) regression line and the grey shaded area shows the 95% confidence interval. Each data point is color coded by the respective species (see legend in upper right panel).

Odonata is a diverse insect order phylogenetically close to the first flying insects, with wingspans, wingbeat frequencies and flight speeds varying significantly across species [54]. Are the classes and positioning of wing mechanosensors consistent across different families of Odonata? And how do sensor systems scale as wing sizes vary across Odonata species? By performing a broad comparison of wing sensor distribution, we can identify key parameters that are conserved, and expression patterns that might hint at specialised functional roles. We imaged the external morphology of wing sensors in 15 species (12 dragonflies and three damselflies) from 10 of the most studied families of odonates by exciting autofluorescence under a confocal microscope. From these images we were able to calculate the local sensor density (sensors/mm) along the wingspan for each species. To facilitate comparison between species, we normalised each density curve by its respective mean. Our analyses focused on three major longitudinal veins near the leading edge: the costa, subcosta and radius, as they contain the most diverse range of sensors and bear most of the load during flight [70,71].

The general rule for sensor placement in the valleys and ridges of the wing corrugation is conserved across the odonates studied (Figure 4A–H). Bristle-bump complexes and campaniform sensilla are positioned on the ridges (ventral side of subcosta and dorsal side of radius) and isolated bristles in the valleys (dorsal side subcosta and ventral side radius). Margin bristle-bump complexes are found in all 15 species (Figure 4A), but bristle-bump complexes (Figure 4C,F), campaniform sensilla (Figure 4B,D,G) and isolated bristles (Figure 4E,H) are missing in some species. The differences across species are most evident on the subcosta, where only dragonfly species express bristle-bump complexes and isolated bristles (Figure 4C,E). It is possible that the external stimuli (for example, flow velocity field, or dynamic strain field) differ across Odonata species due to differences in flight kinematics or the wings' mechanical properties [8,54,72].

On the costa, margin bristle density shows little variation across the wing length for all species on both dorsal and ventral wing surfaces (Figure 4A). However, the damselflies *I. verticalis*, *C. maculata* and the dragonflies *P. tenera*, *S. plagiatus* and *I. stevensi* show local peaks near the nodus (approximately half wing length) on the dorsal side. For all species but *P. gigantea,* sensor densities are higher on the ventral side compared to the dorsal (Table S1). Smaller wings have higher wing margin bristle-bump sensor density, with *I. verticalis*, *P. tenera* and *I. stevensi* having an average density of 7 sensors/mm, 8 sensors/mm and 10 sensors/mm respectively compared to 4 sensors/mm average density for *A. sieboldii* and *H. brevistylus* on the dorsal side of the costa.

The density of campaniform sensilla along the major veins decreases gradually from wing hinge to tip (Figure 4B,D,G). Strain magnitude during flapping also decreases from wing hinge to wing tip, so this reduction in campaniform density might be matched to the dynamic range of sensory input [34]. We also found occasional pairs of campaniform separated by just a few micrometres. These campaniform pairs might be the result of stochastic sensor placement during development, or they could have functional significance. For example, they might provide redundancy or enhanced dynamic range at an important location. Finally, we consistently found at least one dorsal campaniform distal to the pterostigma on the radius vein.

The cross-species comparison also reveals that sensor counts increase with wing length for all three sensor types (Figure 4I–K). Given the data points available, bristle-bump complex (OLS slope 0.89; 95% CI [0.29, 1.5] and isolated bristle (OLS slope 1.42; 95% CI [0.39, 2.45]) counts resemble isometric scaling with wing length, while the campaniform sensilla counts scale faster than the isometric line (OLS slope 1.91; 95% CI [1.18, 2.6]). The number of bristles found on the wing margin of butterfly *P.rapae* (53 bristles, wing length 26mm) [69] does not fit the same scaling relationship found for Odonata, as the number is far below the OLS regression confidence interval found for Odonata. Campaniform sensilla counts on the wing of the grasshopper *Melanoplus sanguinipes* (sensilla count: 54) [64] and the fly *Drosophila melangoster* (sensilla count: 8) [73] are both higher than the OLS regression line for odonates predicts for a wing at that size. In general, this suggests that biomechanics and phylogenetic constraints determine sensor counts and larger wings are not simply a scaled-up version of smaller wings.

The strain distribution on major veins and wing state estimation

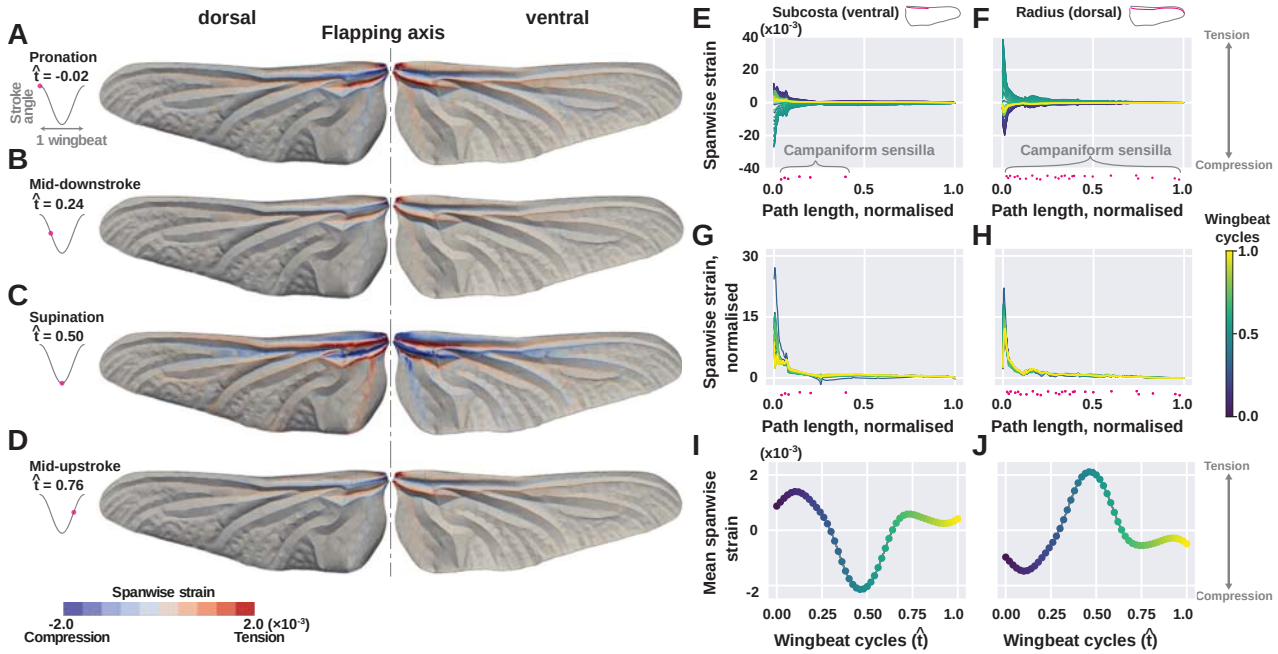

Figure 5. Strain distributions on a simulated flapping wing. **(A–D)** Spanwise strain (spanwise component of normal elastic strain) contour over the wing surface for four time instances in a wing stroke cycle: pronation (**A**), mid-downstroke **(B)**, supination **(C)**, and mid-upstroke **(D)**. A hindwing of a Sympetrum striolatum was reconstructed in 3D for this simulation. **(E,F)** Spanwise strain along ventral subcosta and dorsal radius where campaniform sensilla can be found. The colour map represents different phase of a flapping cycle. **(G,H)** Spanwise strains along the veins, each line is normalised with the mean of the strain along the vein . The x-axis (path length, or position along vein) for the spanwise strains are normalised with the total path length for corresponding vein. **(I,J)** Temporal variation of the mean spanwise strain on the ventral subcosta and dorsal radius. The measured positions of campaniform sensilla are shown in magenta dots **(E-H)**. The vertical variation of the dots is purely for readability.

The state of a rigid wing can typically be described by its angle of attack, airspeed, and the configurations of the control surfaces. A flexible wing is more complicated. For example, as it twists under changes in load, the angle of attack varies along the wingspan with time. The airspeed is also unlikely to be constant. To encode the state of a flexible wing, both strain and flow sensing are likely required. Here we examine a simple scenario of wing deformation and ask how the campaniform sensilla distribution might enable some basic state estimation through strain sensing alone.

Given the structure and material properties of a wing, the strain distribution along the major veins is determined by the sum of inertial and aerodynamic loads. During flapping, inertial loads generally exceed the aerodynamic loads for large insects [23,74]. To encode any aerodynamic components of strain, the wing sensory system must detect small variations of the strain field from the dominant inertial load. Understanding this requires examining wing states and their representative strain distributions on the veins. We generated some possible wing states without the fluid-structure interactions by building a computational solid dynamics (CSD) model of a flapping *S. striolatum* dragonfly wing based on µCT data (see Methods).

The surface spanwise strain contours of four snapshots (Figure 5A–D) show high concentration of strain at the longitudinal veins especially near the wing base. The spanwise strain is greatest at the stroke reversals (Figure 5A,C); the proximal portion of the radius experiences compression (negative strain, in blue) at pronation (Figure 5A), while the same vein experiences tension (positive strain, in red) at supination (Figure 5C). On the other hand, the proximal subcosta and cubitus (two longitudinal veins adjacent to the radius) have the opposite sign. This is because the corrugation offsets some longitudinal veins away from the neutral plane of bending. We also quantified the spanwise strain along two major longitudinal veins (subcosta and radius, Figure 5E–J) where we found campaniform sensilla on their corresponding 'ridge' sides (ventral side for subcostal and dorsal side for radius). These veins show a consistent spatial distribution of strain along their length (Figure 5G,H), but with a large temporal variation in magnitude over the flapping cycle (Figure 5I,J).

How might the wing sensory system encode deformation? Our CSD simulation shows that the wing state can be broken down into two components: 1) the temporal profile of strain magnitude over a flapping cycle (Figure 5I,J); and 2) the nominal spatial profile of strain along each vein (Figure 5G,H). Given a specific set of wing-base kinematics, or flapping mode, the spatial strain profile is stereotyped. Thus only a few campaniform sensilla are required to encode different flapping modes and the magnitude of the profile. However, any deviation from the nominal spatial strain profile provides a signature for the wing deformation state that could be caused by perturbations or altered kinematics (e.g. during manoeuvring). To detect such variation requires higher spatial resolution and dynamic range in strain sensitivity, which can be accomplished by increasing the campaniform count. Specifically, since campaniform function as a strain detector, there are two approaches to encoding high resolution strain values. Firstly, clusters of campaniforms at key locations with different strain thresholds and temporal tuning can collectively cover a range of strain magnitudes. Alternatively, a population of similar campaniforms evenly distributed along the vein can encode the magnitude variation in their activation phase as the deformation travels along the vein. Both approaches require a high campaniform count for high resolution and are not mutually exclusive. While the observed distribution of campaniform is well matched to the general strain magnitude, electrophysiological studies are needed to clarify the encoding approaches. Finally, strain sensing is only half of the story for wing state estimation. Future fluid-structure interaction simulations to illuminate how flow sensing is tuned to the spatial and temporal aerodynamic state of insect wings.

Conclusion

This work provides the most complete map of wing sensory system for a flying animal, from neuron wiring to sensor morphology and distribution. In addition to the comprehensive maps of one dragonfly and one damselfly species, we compared the sensor distribution on the major veins of 15 Odonata species. We have described novel sensors and the cross-species comparison has revealed what appear to be conserved sensor placement themes

in Odonata. Finally, our initial, geometrically precise, structural dynamics modelling generated hypotheses of how the distributed strain sensors monitor wing state. The Odonata wing sensory system is poised to provide information on the wing states in addition to providing inertial state estimation for the body. Our findings have raised several key questions regarding aeroelastic sensing for flight control that will be investigated with neurophysiological experimentation and computational fluid-structure interaction modelling.

Insect wings are underactuated yet extensively sensorised structures. Their venation patterns must not only produce predictable passive mechanical behaviours, but also provide an appropriate substrate to support the number, density, and appropriate positioning of wing sensors in order to observe the relevant biomechanical events during flight. To add yet more complexity, it is both feasible and likely, that the vein substrates are mechanically tuned to amplify, or filter, the response of the sensors they support. This hand-in-glove integration of mechanical behaviour and sensing for state estimation (sometimes termed 'morphological computing' or 'embodied intelligence') makes insect wings an intriguing and tractable model for investigating the co-evolution of form, function, and the nervous system.

Author contributions

HTL & RJB conceived the project and secured funding; JF & HTL performed pilot studies and preliminary mapping; IS performed confocal microscopy, and generated the neuroanatomy maps; IS and MU analysed the sensor distribution data; MM built the wing model and performed the flapping simulation. JF & HTL developed the manuscript; all authors revised the manuscript for submission.

Acknowledgements

We would like to thank the Biotechnology and Biological Sciences Research Council for supporting this work (Grant BB/R002509/1 to HTL and BB/R002657/1 to RJB). We would like to thank Dr Ben Price for lending us selected specimens from the NHM collection. We would like to thank Dr Alexandra Yarger and Dr David Labonte for their valuable feedback on the manuscript. We lament the environmental destruction for housing development at one of our dragonfly sites in SE England.

References

1. Clarac, F., and Dando, M.R. (1973). Tension Receptor Reflexes in the Walking Legs of the Crab Cancer pagurus. Nature *243*, 94–95. 10.1038/243094a0.

2. Dickinson, M.H. (2000). How Animals Move: An Integrative View. Science (80-.). *288*, 100–106. 10.1126/science.288.5463.100.

3. Mischiati, M., Lin, H.-T., Herold, P., Imler, E., Olberg, R., and Leonardo, A. (2015). Internal models direct dragonfly interception steering. Nature *517*, 333–338. 10.1038/nature14045.

4. Lin, H.-T., and Leonardo, A. (2017). Heuristic Rules Underlying Dragonfly Prey Selection and Interception. Curr. Biol. *27*, 1124–1137. 10.1016/j.cub.2017.03.010.

5. Singh, K., and Scott, S.H. (2003). A motor learning strategy reflects neural circuitry for limb control. Nat. Neurosci. *6*, 399–403. 10.1038/nn1026.

6. Bomphrey, R.J., and Godoy-Diana, R. (2018). Insect and insect-inspired aerodynamics: unsteadiness, structural mechanics and flight control. Curr. Opin. Insect Sci. *30*, 26–32. 10.1016/j.cois.2018.08.003.

7. Dickson, W., Straw, A., Poelma, C., and Dickinson, M. (2006). An Integrative Model of Insect Flight Control (Invited). In 44th AIAA Aerospace Sciences Meeting and Exhibit (American Institute of Aeronautics and Astronautics), pp. 431–449. 10.2514/6.2006-34.

8. Combes, S.A., and Daniel, T.L. (2003). Flexural stiffness in insect wings I. Scaling and the influence of wing venation. J. Exp. Biol. *206*, 2979–2987. 10.1242/jeb.00523.

9. Brown, R.E., and Fedde, M.R. (1993). Airflow Sensors in the Avian Wing. J. Exp. Biol. *179*, 13–30.

10. Carruthers, A.C., Thomas, A.L.R., and Taylor, G.K. (2007). Automatic aeroelastic devices in the wings of a steppe eagle Aquila nipalensis. J. Exp. Biol. *210*, 4136–4149. 10.1242/jeb.011197.

11. Sterbing-D'Angelo, S., Chadha, M., Chiu, C., Falk, B., Xian, W., Barcelo, J., Zook, J.M., and Moss, C.F. (2011). Bat wing sensors support flight control. Proc. Natl. Acad. Sci. *108*, 11291–11296. 10.1073/pnas.1018740108.

12. Dickerson, B.H., Aldworth, Z.N., and Daniel, T.L. (2014). Control of moth flight posture is mediated by wing mechanosensory feedback. J. Exp. Biol. *217*, 2301–2308. 10.1242/jeb.103770.

13. Hardie, R.C. (1985). Functional Organization of the Fly Retina. In (Springer, Berlin, Heidelberg), pp. 1–79. 10.1007/978-3-642-70408-6_1.

14. Samonds, J.M., Geisler, W.S., and Priebe, N.J. (2018). Natural image and receptive field statistics predict saccade sizes. Nat. Neurosci. *21*, 1591–1599. 10.1038/s41593-018-0255-5.

15. Ruppel, G. (1989). Kinematic Analysis of Symmetrical Flight Manoeuvres of Odonata. J. Exp. Biol. *144*, 13–42.

16. Thomas, A.L.R. (2004). Dragonfly flight: free-flight and tethered flow visualizations reveal a diverse array of unsteady lift-generating mechanisms, controlled primarily via angle of attack. J. Exp. Biol. *207*, 4299–4323. 10.1242/jeb.01262.

17. Gettrup, E. (1966). Sensory regulation of wing twisting in locusts. J. Exp. Biol. *44*, 1–16.

18. Wilson, B.Y.D.M. (1961). The Central Nervous Control of Flight in a Locust. J. Exp. Biol. *38*, 471–490.

19. Dickinson, M.H. (1990). Comparison of Encoding Properties of. J. Exp. Biol. *151*, 245–261.

20. Yarger, A.M., and Fox, J.L. (2018). Single mechanosensory neurons encode lateral displacements using precise spike timing and thresholds. Proc. R. Soc. B Biol. Sci. *285*, 20181759. 10.1098/rspb.2018.1759.

21. Pringle, J.W.S. (1948). The Gyroscopic Mechanism of the Halteres of Diptera. Philos. Trans. R. Soc. B Biol. Sci. *233*, 347–384.

22. Pratt, B., Deora, T., Mohren, T., and Daniel, T. (2017). Neural evidence supports a dual sensory-motor role for insect wings. Proc. R. Soc. B Biol. Sci. *284*, 20170969. 10.1098/rspb.2017.0969.

23. Jankauski, M., Daniel, T.L., and Shen, I.Y. (2017). Asymmetries in wing inertial and aerodynamic torques contribute to steering in flying insects. Bioinspiration and Biomimetics *12*, 046001. 10.1088/1748-3190/aa714e.

24. Eberle, A.L., Dickerson, B.H., Reinhall, P.G., and Daniel, T.L. (2015). A new twist on gyroscopic sensing: Body rotations lead to torsion in flapping, flexing insect wings. J. R. Soc. Interface *12*. 10.1098/rsif.2014.1088.

25. Hinson, B.T., and Morgansen, K.A. (2015). Gyroscopic sensing in the wings of the hawkmoth Manduca sexta : the role of sensor location and directional sensitivity. Bioinspir. Biomim. *10*, 056013. 10.1088/1748-3190/10/5/056013.

26. Dickinson, M.H., and Palka, J. (1987). Physiological properties, time of development, and central projection are correlated in the wing mechanoreceptors of Drosophila. J. Neurosci. *7*, 4201–4208. 10.1523/jneurosci.07-12-04201.1987.

27. Rajabi, H., Schroeter, V., Eshghi, S., and Gorb, S.N. (2017). The probability of wing damage in the dragonfly Sympetrum vulgatum (Anisoptera: Libellulidae): a field study. Biol. Open *6*, 1290–1293. 10.1242/bio.027078.

28. Kondo, H. (1978). Efferent system of the lateral ocellus in the dragonfly: Its relationships with the ocellar afferent units, the compound eyes, and the wing sensory system. J. Comp. Physiol. □ A *125*, 341–349. 10.1007/BF00656869.

29. Simmons, P. (1977). The neuronal control of dragonfly flight. I. Anatomy. J. Exp. Biol. *71*, 123–140. 10.25911/5d7783acf1631.

30. Rajabi, H., Moghadami, M., and Darvizeh, A. (2011). Investigation of microstructure, natural frequencies and vibration modes of dragonfly wing. J. Bionic Eng. *8*, 165–173. 10.1016/S1672-6529(11)60014-0.

31. Gao, C.-Y., Meng, G.-X., Li, X., Wu, M., Liu, Y., Li, X.-Y., Zhao, X., Lee, I., and Feng, X. (2013). Wettability of dragonfly wings: the structure detection and theoretical modeling. Surf. Interface Anal. *45*, 650–655. 10.1002/sia.5105.

32. Yoshida, A., and Emoto, J. (2011). Variations in the Arrangement of Sensory Bristles along Butterfly Wing Margins. Zoolog. Sci. *28*, 430–437. 10.2108/zsj.28.430.

33. Li, J., Zhang, W., Guo, Z., Wu, S., Jan, L.Y., and Jan, Y.-N. (2016). A Defensive Kicking Behavior in Response to Mechanical Stimuli Mediated by Drosophila Wing Margin Bristles. J. Neurosci. *36*, 11275–11282. 10.1523/JNEUROSCI.1416-16.2016.

34. Houot, B., Gigot, V., Robichon, A., and Ferveur, J.-F. (2017). Free flight odor tracking in Drosophila: Effect of wing chemosensors, sex and pheromonal gene regulation. Sci. Rep. *7*, 40221. 10.1038/srep40221.

35. Fabian, J.M., el Jundi, B., Wiederman, S.D., and O'Carroll, D.C. (2020). The complex optic lobe of dragonflies. bioRxiv, 2020.05.10.087437. 10.1101/2020.05.10.087437.

36. Piersanti, S., Frati, F., Conti, E., Gaino, E., Rebora, M., and Salerno, G. (2014). First evidence of the use of olfaction in Odonata behaviour. J. Insect Physiol. *62*, 26–31. 10.1016/j.jinsphys.2014.01.006.

37. Camhi, J.M. (1969). Locust wind receptors. I. Transducer mechanics and sensory response. J. Exp. Biol. *50*, 335–348.

38. Bacon, J., and Tyrer, M. (1979). The innervation of the wind-sensitive head hairs of the locust, Schistocerca gregaria. Physiol. Entomol. *4*, 301–309. 10.1111/j.1365-3032.1979.tb00621.x.

39. Pflüger, H.-J., and Wolf, H. (2013). Developmental and activity-dependent plasticity of filiform hair receptors in the locust. Front. Physiol. *4*, 1–7. 10.3389/fphys.2013.00070.

40. McCorkell, F. (2016). Aerodynamic flow sensing in the desert locust (Schistocerca gregaria).

41. Simmons, P.J. (1978). Crevice organs: Sensory structures on the wings of dragonflies (Insecta, Odonata). Zoomorphologie *89*, 251–255. 10.1007/BF00993951.

42. Spinola, S.M., and Chapman, K.M. (1975). Proprioceptive indentation of the campaniform sensilla of cockroach legs. J. Comp. Physiol. ? A *96*, 257–272. 10.1007/BF00612698.

43. Vincent, J.F. V., Clift, S.E., and Menon, C. (2007). Biomimetics of campaniform sensilla: Measuring strain from the deformation of holes. J. Bionic Eng. *4*, 63–76. 10.1016/S1672-6529(07)60015-8.

44. Zill, B.Y.S.N., and Moran, D.T. (1981). The Exoskeleton and Insect Proprioception. I. Responses of Tibial Campaniform Sensilla to External and Muscle-Generated Forces in the American Cockroach, Periplaneta Americana. J. Exp. Biol. *91*, 1–24.

45. Cole, E.S., and Palka, J. (1982). The pattern of campaniform sensilla on the wing and haltere of Drosophila melanogaster and several of its homeotic mutants. J. Embryol. Exp. Morphol. *Vol. 71*, 41–61.

46. Field, L.H., and Matheson, T. (1998). Chordotonal Organs of Insects. In Advances in Insect Physiology (Academic Press Inc.), pp. 1–228. 10.1016/S0065-2806(08)60013-2.

47. Wolfrum, U. (1990). Actin filaments: the main components of the scolopale in insect sensilla. Cell Tissue Res. *261*, 85–96. 10.1007/BF00329441.

48. Kutsch, W., Hanloser, H., and Reinecke, M. (1980). Light- and electron-microscopic analysis of a complex sensory organ: The tegula of Locusta migratoria. Cell Tissue Res. *210*, 461–478. 10.1007/BF00220202.

49. Burrows, M. (1996). The Neurobiology of an Insect Brain (Oxford University Press) 10.1093/acprof:oso/9780198523444.001.0001.

50. Wootton, R.J. (1998). Smart Engineering in the Mid-Carboniferous: How Well Could Palaeozoic Dragonflies Fly? Science (80-.). *282*, 749–751. 10.1126/science.282.5389.749.

51. Norris, A.G., Palazotto, A.N., and Cobb, R.G. Structural Dynamic Characterization of an Insect Wing Toward the Development of "Bug-Sized" Flapping-Winged Micro Air Vehicles. 10.2514/6.2010-2790.

52. Jongerius, S.R., and Lentink, D. (2010). Structural Analysis of a Dragonfly Wing. Exp. Mech. *50*, 1323–1334. 10.1007/s11340-010-9411-x.

53. Wang, J.K., and Sun, M. (2005). A computational study of the aerodynamics and forewing-hindwing

interaction of a model dragonfly in forward flight. J. Exp. Biol. *208*, 3785–3804. 10.1242/jeb.01852.

54. Bomphrey, R.J., Nakata, T., Henningsson, P., and Lin, H.-T. (2016). Flight of the dragonflies and damselflies. Philos. Trans. R. Soc. B Biol. Sci. *371*, 20150389. 10.1098/rstb.2015.0389.

55. Li, C., and Dong, H. (2017). Wing kinematics measurement and aerodynamics of a dragonfly in turning flight. Bioinspir. Biomim. *12*, 026001. 10.1088/1748-3190/aa5761.

56. Bode-Oke, A.T., Zeyghami, S., and Dong, H. (2017). Aerodynamics and flow features of a damselfly in takeoff flight. Bioinspir. Biomim. *12*, 056006. 10.1088/1748-3190/aa7f52.

57. Bode-Oke, A.T., Zeyghami, S., and Dong, H. (2018). Flying in reverse: kinematics and aerodynamics of a dragonfly in backward free flight. J. R. Soc. Interface *15*, 20180102. 10.1098/rsif.2018.0102.

58. Hefler, C., Qiu, H., and Shyy, W. (2018). Aerodynamic characteristics along the wing span of a dragonfly Pantala flavescens. J. Exp. Biol. *221*, jeb171199. 10.1242/jeb.171199.

59. Shumway, N., Gabryszuk, M., and Laurence, S. (2020). The impact of dragonfly wing deformations on aerodynamic performance during forward flight. Bioinspir. Biomim. *15*, 026005. 10.1088/1748-3190/ab597e.

60. Frantsevich, L., Gorb, S., Radchenko, V., Gladun, D., and Polilov, A. (2014). Lehr's fields of campaniform sensilla in beetles (Coleoptera): Functional morphology. I. General part and allometry. Arthropod Struct. Dev. *43*, 523–535. 10.1016/j.asd.2014.09.001.

61. Jensen, H. (1976). Ultrastructure of the aortic diverticula of the adult dragonfly Sympetrum danae (Odonata: anisoptera). Cell Tissue Res. *168*, 177–191. 10.1007/BF00215876.

62. Pass, G. (2018). Beyond aerodynamics: The critical roles of the circulatory and tracheal systems in maintaining insect wing functionality. Arthropod Struct. Dev. *47*, 391–407. 10.1016/j.asd.2018.05.004.

63. Salcedo, M.K., and Socha, J.J. (2020). Circulation in Insect Wings. Integr. Comp. Biol. *60*, 1208–1220. 10.1093/icb/icaa124.

64. Albert, P.J., Zacharuk, R.Y., and Wong, L. (1976). Structure, innervation, and distribution of sensilla on the wings of a grasshopper. Can. J. Zool. *54*. 10.1139/z76-178.

65. Altman, J.S., Anselment, E., and Kutsch, W. (1978). Postembryonic development of an insect sensory system: Ingrowth of axons from hindwing sense organs in Locusta migratoria. Proc. R. Soc. London - Biol. Sci. *202*, 497–516. 10.1098/rspb.1978.0082.

66. Mohren, T.L., Daniel, T.L., Brunton, S.L., and Brunton, B.W. (2018). Neural-inspired sensors enable sparse, efficient classification of spatiotemporal data. Proc. Natl. Acad. Sci. U. S. A. *115*, 10564–10569. 10.1073/pnas.1808909115.

67. Koehler, C., Liang, Z., Gaston, Z., Wan, H., and Dong, H. (2012). 3D reconstruction and analysis of wing deformation in free-flying dragonflies. J. Exp. Biol. *215*, 3018–3027. 10.1242/jeb.069005.

68. Ai, H., Yoshida, A., and Yokohari, F. (2010). Vibration receptive sensilla on the wing margins of the silkworm moth Bombyx mori. J. Insect Physiol. *56*, 236–246. 10.1016/j.jinsphys.2009.10.007.

69. Yoshida, A., Noda, A., and Emoto, J. (2001). Bristle distribution along the wing margin of the small white cabbage butterfly (Lepidoptera: Pieridae). Ann. Entomol. Soc. Am. *94*, 467–470. 10.1603/0013-8746(2001)094[0467:BDATWM]2.0.CO;2.

70. Büsse, S., and Hörnschemeyer, T. (2013). The thorax musculature of Anisoptera (Insecta: Odonata) nymphs and its evolutionary relevance. BMC Evol. Biol. *13*, 237. 10.1186/1471-2148-13-237.

71. Wootton, R. (1992). Functional Morphology Of Insect Wings. Annu. Rev. Entomol. *37*, 113–140. 10.1146/annurev.ento.37.1.113.

72. Rajabi, H., and Gorb, S.N. (2020). How do dragonfly wings work? A brief guide to functional roles of wing structural components. Int. J. Odonatol. *23*, 23–30. 10.1080/13887890.2019.1677515.

73. Dickinson, M., and Palka, J. (1987). Physiological properties, time of development, and central projection are correlated in the wing mechanoreceptors of Drosophila. J. Neurosci. *7*, 4201–4208. 10.1523/JNEUROSCI.07-12-04201.1987.

74. Combes, S.A. (2003). Flexural stiffness in insect wings II. Spatial distribution and dynamic wing bending. J. Exp. Biol. *206*, 2989–2997. 10.1242/jeb.00524.

75. Riek, E.F., and Kukalová-Peck, J. (1984). A new interpretation of dragonfly wing venation based upon Early Upper Carboniferous fossils from Argentina (Insecta: Odonatoidea) and basic character states in pterygote wings. Can. J. Zool. *62*, 1150–1166. 10.1139/z84-166.

76. Bechly, G. (1995). Morphologische Untersuchungen am Flügelgeäder der rezenten Libellen und deren Stammgruppenvertreter (Insecta; Pterygota; Odonata) unter besonderer Berücksichtigung der Phylogenetischen Systematik und des Grundplanes der *Odonata. Petalura *special-volume*.

Supplemental methods

Insect specimens

All Odonata specimens were collected in northern Virginia, USA (*), south-east England, UK (**), or obtained from the collection at the Natural History Museum in London, UK. They belong to two suborders: first, Anisoptera, the dragonflies, of which there are 13 families; members of the nine most populous/largest were studied here: 1. Aeshnidae, *Anax junius* (Drury, 1773)*, 2. Chlorogomphidae, *Chlorogompus atkinsonii* (Fraser, 1925), 3. Cordulegastridae, *Anotogaster seiboldii* (Selys, 1854), 4. Corduliidae, *Hemicordulia tau* (Selys, 1871), 5. Gomphidae, *Hagenius brevistylus* (Selys, 1854) and *Stylyrus plagiatus* (Selys, 1854)*, 6. Macromiidae, *Macromia indica* (Frasner, 1924), 7. Libellulidae, *Pantala flavescens* (Fabricius, 1798)*, *Perithemis tenera* (Say, 1840)*and *Sympetrum striolatum* (Charpentier, 1840)**, 8. Petaluridae, *Petalura gigantea* (Leach. 1815), 9. Synthemistidae, *Idionyx stevensi* (Fraser, 1924). Second, Zygoptera, the damselflies, of which there are 35 families. The damselflies used here were from the 1. Calopterigidae, *Calopteryx maculata* (Palisot de Beauvois, 1807)* and 2. Coenagrionidae, *Argia apicalis* (Say, 1840)* and *Ischnura verticalis* (Say, 1839)*. We used males in all our analyses, except for *P. tenera*, for which we used both males and females. In this species, the male wings are ~10% shorter and have ~20% more cross-veins than female wings. However, since most wing sensors are located on the longitudinal veins, the sexual dimorphism is not included in the discussion.

Sample preparation for confocal imaging

Neurobiotin diffuses at a rate of ~1 cm/24 hr in axons of the diameter found in the Odonata wing, and insect tissue deterioration begins at approximately 48 hr postmortem. Thus, we focused our efforts on one of the smallest Anisoptera, *P. tenera*, and an Isoptera, *A. apicalis*, with comparable wingspan.

Insects were anesthetized on ice and fixed right side up on Sylgard-filled Petri dishes using pins. The right pterothoracic pleural wall and the head were removed, anterior nerves (nerves 1C and 2C in [S1]) were isolated, placed in a drop (~ 0.7 µl) of distilled water inside a petroleum jelly bowl, and cut. Water was wicked away, replaced with ~0.5 µl of the tracer solution (2 % w/v neurobiotin in dH_2O, Vector Labs, SP-1120) and the well was sealed closed with petroleum jelly. Insects were kept refrigerated in a humid chamber for 48 hours to allow diffusion of the tracer. The wings were removed by cutting along the basal hinge and fixed in 2% PFA in phosphate-buffered saline with 0.1% Triton X-100 (PBS-T) overnight at 4°C with mild agitation, washed with PBS-T and bleached in 20% peroxide in PBS-T for 48 hr to remove most of the pigment from the cuticle.

When wings from young adults (few hours post-eclosion) were used, oxygen from bleaching formed within the bilayer of cuticle making up the wing blade. This can be explained by the presence of metabolites between the unfused sheets of exoskeleton reacting to the peroxide. At the end of bleaching cycle (indicated by the cuticle's pale golden hues) the wings became fully inflated by the oxygen. The wings were briefly rinsed in copious amount of water, and placed inside a vacuum desiccator in a PBS-T-filled Petri dish. The low vacuum caused further delamination of the cuticular bilayer. The gas escaped via the openings at the wing base or, occasionally raptured the trailing edge seam. The wings were cut chordwise in half, post-fixed in 2 % PFA for 3 h @ RT, washed and stained with DyLight 594-NeutrAvidin (1:250, Thermo Scientific #22842). The staining reagent now had free/unencumbered access to the neurobiotin-labelled neurons, in PBS with 3% normal goat serum, 1% triton X-100, 0.5% DMSO @ RT with agitation for 2 days. Following washing with PBS-T, the wings were cut near their base and mounted in Tris-buffered (50 mM, pH 8.0) 80% glycerol with 0.5 % DMSO between two coverslips using 350 µm spacers. The wing bases were dehydrated in glycerol (5-80 %), then ethanol (25-100 %), cleared and mounted in methyl salicylate, following modified protocol from [S2].

For treatments of old wing specimens, samples were bleached and re-hydrated using alkaline peroxide (25% H_2O_2, 0.2% KOH in water) for 24-48 h and mounted in Tris-buffered (50 mM, pH 8.0) 80% glycerol with 0.5 % DMSO between two 60 mm-long coverslips. The mounting followed the same procedure as fresh wings.

Imaging and sensor distribution/placement mapping

All samples were imaged on Zeiss 880 upright confocal microscope. Serial optical sections were obtained at 7 µm with a FLUAR 5x/0.25 NA, 2.5 µm with a Plan-Apochromat 10x/0.45 NA objective, at 1.5 µm with a LD-LCI 25x/0.8 NA objective or at 0.5 µm with a Plan-Apochromat 40x/0.8 NA objective. Cuticle autofluorescence and DyLight 594-NeutrAvidin were imaged using 488 and 594 nm laser lines, respectively. The volumes obtained with the FLUAR 5x objective and tiling the wings were stitched in Fiji (http://fiji.sc/). Images were processed in Fiji, Icy (http://icy.bioimageanalysis.org/) and Photoshop (Adobe Systems Inc.).

The costa, radius and subcosta veins were scanned dorsally and ventrally with Plan-Apochromat 10x/0.45 NA objective (field of view 1.2 x 1.2 mm). To minimize collection time while maintaining high signal to noise ratio, the green autofluorescence of cuticle was excited with 405 and 488 nm lasers at maximum power and the images were collected using single-swipe and minimum pixel dwell time. The vertical aspect of each volume was adjusted to accommodate the imaged vein while the horizontal was kept constant at 1500 pixels. Maximum intensity projections were stitched manually in Photoshop and annotated in Adobe Illustrator (Adobe Systems Inc.) while referring to the volumes viewed in Fiji [S3].

Assessment of backfill efficacy

To assess the completeness of neurobiotin labelling, we focused on the hind wing trailing edge bristles, as they are innervated by the longest axons (most challenging) and hence good indicators of labelling efficacy. We found that within 4.4mm stretch the sensory neurons innervating the bristles of the proximal half of trailing edge (i.e., axons passing through anal and cubitus posterior veins along with their tributaries) were all labelled (fig S1 D, top). However, within the distal 5.8 mm stretch of the trailing edge (i.e. axons traveling through media, radius veins and associated cross-veins), 2/23 dorsal and 4/33 ventral sensory neurons were not labelled (89.3 % efficacy) (Fig S1 D, bottom). Projecting from the full labelling of the proximal half, we accounted for this ~10% dropout at the distal portion.

Wing sensor distribution quantifications

Based on the annotations, sensors were counted and their positions digitized in Fiji. The sensor density was defined as the inverse of the averaged sensor spacing over two consecutive sensors (sensors/mm). The sensor position was normalised with the wing length for comparison across species. Sensor density was first smoothed by a moving average over 7 data points and subsequently normalised by the mean sensor density of the respective sensor type on the vein. Finally, the mean of all species was taken for each sensor type to compare sensor density curves across sensor type and veins.

The relationship between sensor count and wing length for each sensor type was analysed via an ordinary least squares (OLS) regression in Rstudio (Rstudio Team, 2020). The lower and upper confidence intervals (2.5% and 97.5%) of the OLS regression were calculated. In this analysis, the sensor count for each sensor type corresponded to the sum of the sensors of the first three anterior veins (costa, subcosta and radius).

Wing geometry modelling for strain field evaluation

A male *Sympetrum striolatum* dragonfly was euthanised in a freezer overnight. The entire body was stained by elemental iodine, which also had a desiccating effect [S4]. The x-ray microtomography (µCT) scanning on the left hindwing was performed using a SkyScan 1172 scanner (Bruker, Belgium). The wing

was mounted with the long axis vertical, aligned to the rotational axis of the scanner, and five sub-scans were performed. In total, 12445 images were taken at pixel size of 2.83 µm and exposure time of 2.6 s, with a rotation step of 0.08° for 180° rotation for each sub-scan. The source voltage and current were 65 kV and 153 µA, respectively. The raw images were processed in Bruker NRecon to obtain cross-sectional slices. The images were then imported to ORS Dragonfly v3.6 (Object Research Systems, Canada) for registration and three-dimensional reconstruction. A mesh file (PLY) was extracted by choosing an appropriate intensity threshold. After cleaning and reduction in MeshLab, the mesh was imported to Rhinoceros 6 (Robert McNeel & Associates, USA). The vein network was approximated with circular cross-section pipes whose diameter and joint positions were informed from the mesh. The membrane was generated for each cell surrounded by veins with uniform thickness of 10 µm, which was determined by sampling the measured cross section using the Dragonfly software. The veins and membranes were imported into AutoDesk Inventor Professional 2020 (Autodesk, Inc., USA) to merge them into a single body. The wing model was exported in STEP format and imported into ANSYS Mechanical Application 2019 R3 (ANSYS, Inc., USA), where the mesh for finite element analysis was generated for transient structural simulations.

Wing flapping computational solid dynamics (CSD) simulation

The transient structural simulation was performed with ANSYS Mechanical Application 2019 R3. The wing model mesh consists of quadratic tetrahedron elements. The uniform material property was assumed for simplicity, where density was 1200 kg m^{-3}, Poisson ratio was 0.3, and the Young's modulus was 5 GPa. These values were derived from previous work [S5], where the Young's moduli were 6 GPa for vein and 3.75 GPa for membrane. The "remote displacement" boundary condition was applied at the wingbase surface, where only 1 degree of freedom for rotation around the flapping axis (Figure 5A–D) was prescribed for simulating the dominant flapping motion, and other 5 (3 translational and 2 rotational) degrees of freedom were fixed. The flapping motion is described as:

$$\phi = \phi_0 \sin(2\pi t f)\,(1 - e^{-\gamma t})$$

where ϕ is positional angle given at the wingbase in degrees (Figure S3D, blue line), ϕ_0 is the desired wingbeat semi-amplitude and set to 30°, t is time in seconds, f is wingbeat frequency and set to 40 Hz, and γ is a factor to change how fast the amplitude approaches to ϕ_0. The wingbeat amplitude increases gradually in this formulation so we can avoid the abrupt start and it is expected to arrive at the periodic deformation state earlier than a simple sinusoidal flapping. The factor γ was set to 30, which results in the wingbeat amplitude is 30% of ϕ_0 for the 1st cycle but 67%, 84%, and 93% for 2nd, 3rd, and 4th cycles, respectively. At 10th cycle the amplitude is 99.9% of ϕ_0. The wing started flapping from the mid-downstroke phase at time $t = 0$, and the computation was performed until time $t = 16T = 0.4$ s, where $T = 1/f$ was the wingbeat period (i.e. 0.025 s). The time step size (time increment, Δt) for each computational step was determined to be 3×10^{-4} s after several preliminary trials. No external forces such as gravitational force or aerodynamic force were considered in this analysis.

The positional angle was defined such that the original attitude at mid-downstroke is 0, and negative angle at supination and positive angle at pronation. The wingtip path and wing positional angle at the wingtip were calculated for troubleshooting.

Mesh convergence check

Coarse and fine meshes were generated for mesh convergence verification, where coarse mesh has 845,039 nodes while the fine mesh has 1,226,124 nodes (Figure S3A,B). They showed slightly different low-frequency oscillation patterns in the wingtip positional angles (Figure S3C–H). For fair comparison, we took the wingbeat cycles where the mean positional angle during downstroke is the smallest for each case (25th cycle for coarse mesh and 30th cycle for fine mesh, figure S3G,H). The spanwise strains in both

meshes showed good agreement (Figure S3I). Thus we can confirm simulation convergence and show the results from fine mesh alone.

Strain analysis

The resultant strain field was evaluated in two ways: the normal elastic strain along two major longitudinal veins (ventral side of subcosta and dorsal side of radius), and the normal elastic strain contours on the wing surface at four time instants (pronation, mid-downstroke, supination, and mid-upstroke). Here, the normal elastic strain was computed for the wing radial direction for each instant by coordinate transformation using the instantaneous positional angle. We will refer this strain component as "spanwise strain" for short.

The period of low-frequency oscillation for the fine mesh case was around 8-10 wingbeat cycles (Figure S3D,F,H). The strain along two veins for one low-frequency period (from the 22nd to 30th wingbeat cycles) showed some variation but the general trend was consistent, where the mean spanwise strain for the ventral subcosta and the dorsal radius show opposing temporal patterns (Figure S3J,K,L). Therefore, in the main text, we show the representative results from the 28th wingbeat cycle starting from pronation (i.e., $27.75 \leq t/T \leq 28.75$). For simplicity, each wingbeat cycle was described with $\hat{t}$ such that $0 \leq \hat{t} \leq 1$, where $\hat{t}=0$ and 1 are pronation and $\hat{t}=0.5$ is supination. The spanwise strain along two veins were analysed in three ways. The raw strain along each vein for each instant was plotted (Figure 5E,F); the raw strain was normalised with the mean along the vein at the corresponding time (Figure 5G,H); and the mean strain was plotted against time. This way, we expected to see if the time-varying strain distribution can be decomposed into spatial and temporal components.

The spanwise strain contours on the surface were calculated in ANSYS CFD-Post 2019 R3. The mesh and strain for each time instance was exported in a Generic format using Command Editor with simple for-loop. The files and converted into VTK (legacy) format with a custom-written Python script and imported into ParaView 5.9.0 (KitWare, Inc., USA) for visualisation.

Modelling limitations

To our knowledge, this wing model is the most geometrically detailed insect wing to date, yet the model and the simulation both have some limitations. The material properties (in particular the Young's modulus) is uniform over the entire wing; no elastic joints are implemented (in particular nodus); cross-sectional shapes of the veins are circular and filled (in reality, it is hollow and more elliptic in dorsoventral direction); and the wing kinematics at the wing base were simplified to a sinusoidal curve around single-axis, whereas active pitching rotation occurs in real-life. Nevertheless, this current model already illustrates some general patterns necessary to infer how aeroelastic wing state can be encoded. We will continue to improve the model fidelity in future work.

Supplemental figures and table

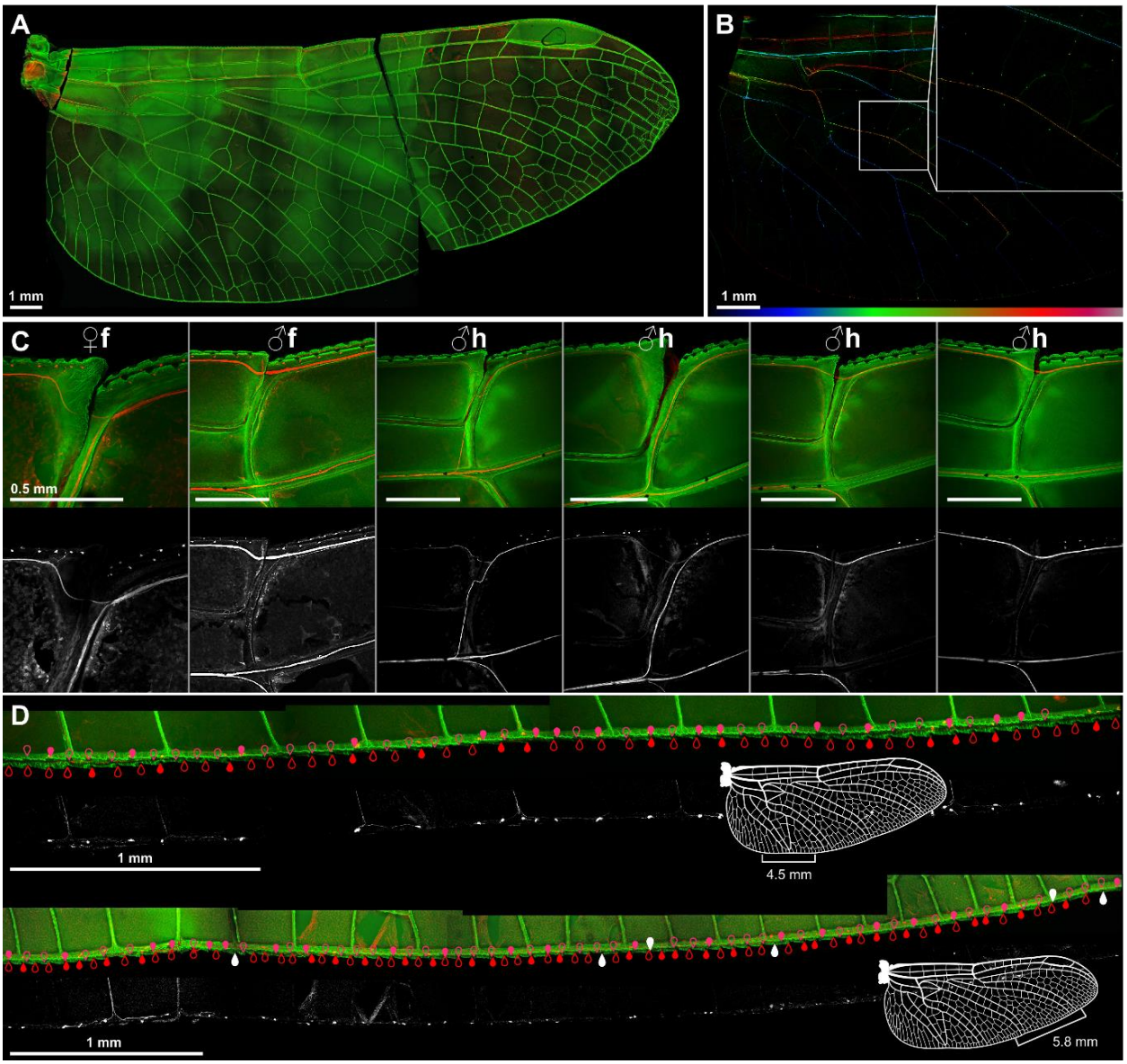

Supplemental Figure 1. (A) *P. tenera* hind wing maximum intensity projection of stitched volumes collected with the FLUAR 5x objective. Cuticle autofluorescence – green; DyLight 594-neutroavidin – red. **(B)** Depth color-coded projection of the red channel. Cell bodies of various sensors appear as dots. **(C)** Variability of the axonal track passage at the nodus of *P. tenera*: axons of the leading-edge wing margin sensors distal to nodus may continue down the costa or take an alternative path down the radius vein. The variability occurs in both sexes fore (f) and hind (h) wings. **(D)** Assessment of the efficiency of the backfill using *P. tenera* hind wing margin bristle-bump complexes on the trailing edge as a proxy. Filled markers indicate labelled cell bodies; empty markers – bumps not accompanied by a bristle; white markers: unlabeled cell bodies (bristle present, lack of detectable signal from the cell body).

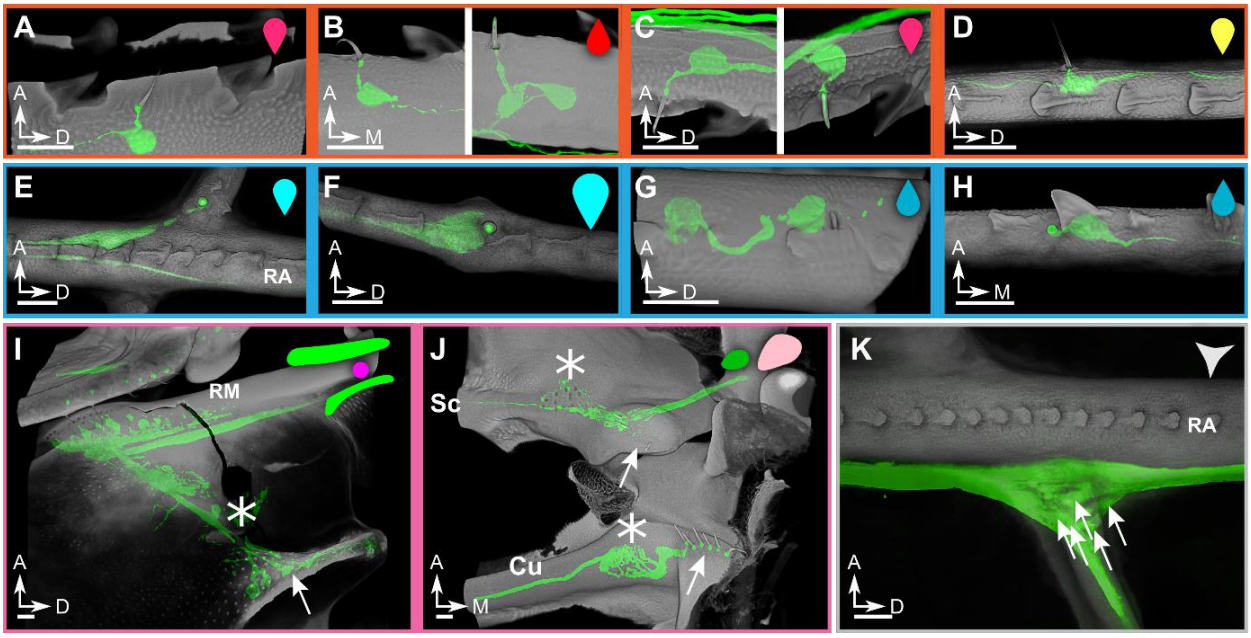

Supplemental Figure 2. Examples of wing veins and base sensors of damselfly *Argia apicalis*. Most structures are analogous to the dragonfly. **(A-D)** air flow sensors; **(A)** dorsal costa bristle-bump complex; **(B)** ventral costa bristle-bump complex; left: single-innervated; right: double-innervated bristle. **(C)** trailing edge bristle-bump complex; left: single-innervated; right: double-innervated bristle. **(D)** short isolated bristle. **(E-H):** strain sensors; (**E**) Campaniform sensilla (CS) of a cross veinvein medial to pterostigma; (**F**) large dorsal radius anterior CS immediately distal to pterostigma; **(G)** ventral media CS proximal to the wing base; (**H**) one of ventral media posterior CS. **(I-K)** wing base sensors. **(I)** crevice organ (i.e. campaniform sensilla) – two parallel fields of directionally tuned/elongated CS dorsally at the base of radius/media (RM) vein. Asterisk marks the dorsal insertion site of a wing base chordotonal organ. Arrow – CS field of axillary complex posterior ridge. **(J)** Ventral view of the subcostal and cubitus vein base. Arrows point to hair plates, asterisks mark CS fields. **(K)** Multipolar receptor at the junction of radius and a cross vein posterior to the nodus. Arrows point to several large cell bodies. All the images show mechanosensors of the right forewing. Cuticle's autofluorescence shown in grey, neurons labelled with Neurobiotin/DyLight-594-Neutravidin – in green. Scale bars: 25 µm. The symbols in the upper right corner of each panel correspond to the markers showing placement of sensors in Fig. 3.

	Mean sensor density (1/mm)												Wing length (mm)	Sensor count
	C(d)		Sc(d)	R(d)			C(v)		Sc(v)			R(v)		
Species	**cs**	**bb**	**is**	**cs**	**bb**	**sis**	**cs**	**bb**	**cs**	**bb**	**sis**	**is**		
I.verticalis		6.69						9.64					1.15	202
P.tenera		7.81	5.58	2.2	2.92			11.98	10.73			3.71	2.07	519
A.apicalis		2.95						5.94					2.46	168
S.striolatum	1.45	4.99	3.78	1.06	2.65			7.83		2.19		3.45	2.95	547
C.maculata		4.93				6.71	2.27	8.86					3.06	392
I.stevensi	1.94	10.63	3.75	1.33	2.48			15.57	6.71	3.88		11.19	3.31	1080
H.tau	2.38	5.5	7.24	1.45	2.7			9.12	4.46	2.39		12.16	3.63	734
S.plagiatus	3.08	4.01		5.52	1.5		2.10	6.21	7.18	1.45			3.74	600
C.atkinsoni	2.55	5.18		6.96	2.48		4.25	8.74	6.69			12.64	4.05	900
P.flavescens	1.16	4.94	12.37	1.06	2.37			7.73		2.63		14.41	4.33	844
M.indica	1.11	6.72		2.86	3.27			15.18	3.37	3.05		7.3	4.76	1420
A.junius		5.47	2.99	2.35	2.24		2.83	6.47	5.08	2.2		7.55	5.36	1065
P.gigantea	2.98	4.22		5.36	2.00		3.58	4.02	7.38	1.43	0.98	4.45	5.41	793
A.sieboldii	2.34	3.93	1.64	5.49	1.99	3.73	1.75	7.26	6.99		1.64		5.44	958
H.brevistylus	1.77	3.93	2.03	3.98	1.81	2.62	2.63	6.55	5.81		2.03		5.45	766

Supplemental Table 1. Mean sensor density, wing length and sensor count of 15 Odonata species. Mean sensor density and sensor counts are presented for the three major longitudinal veins Costa (C), Subcosta (Sc) and Radius (R) on dorsal (d) and ventral (v) wing side. Mean sensor density is presented for campaniform sensilla (cs), isolated bristles (is), bristle-bump complexes (bb) and small bristles in the range of a bump (sis). The last sensor type was assigned to the bristle-bump complexes in the article because the bristles had the same morphology and could be associated to a nearby cuticular bump.

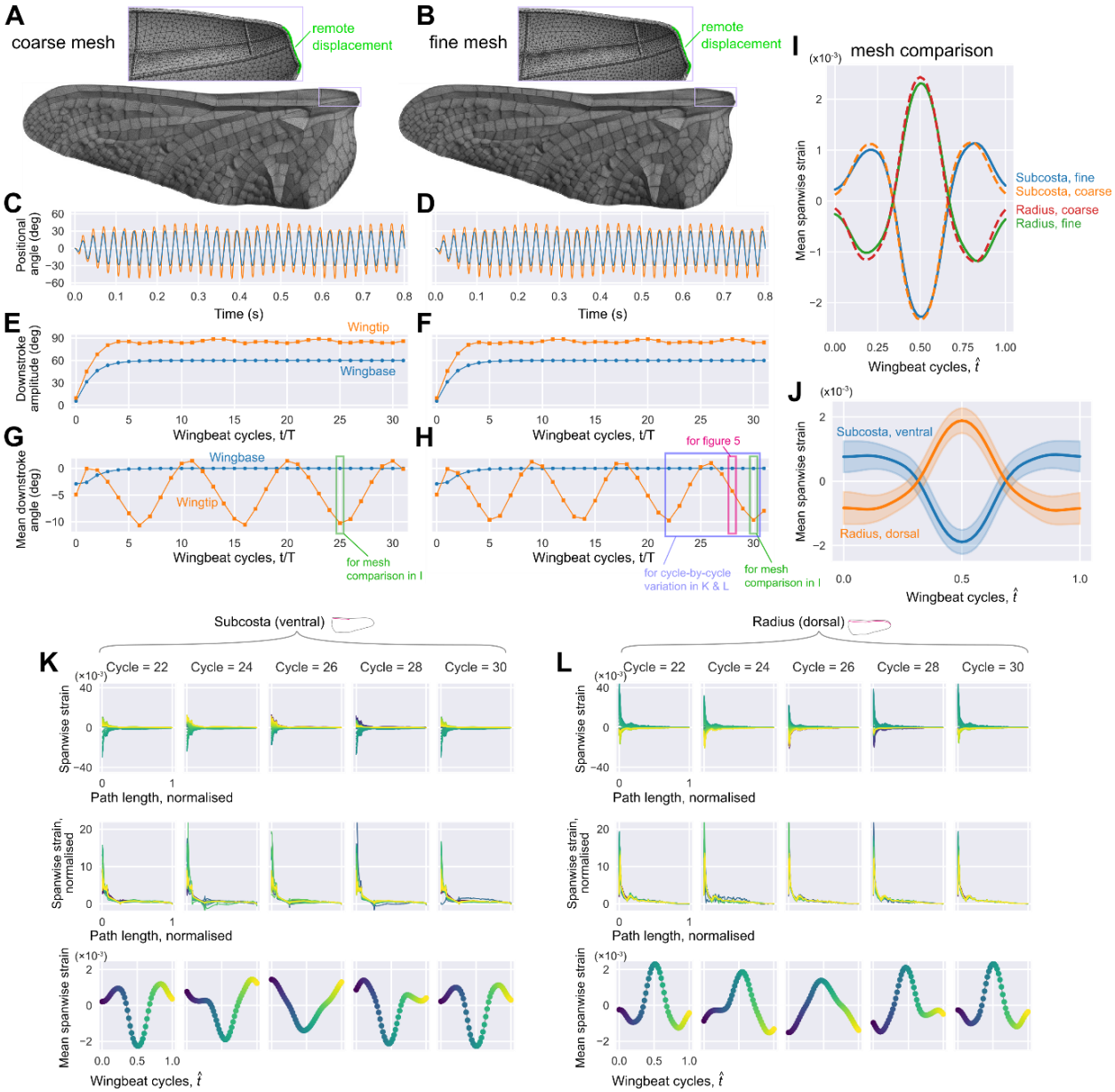

Supplemental Figure 3. Mesh convergence and cycle-by-cycle variation in spanwise strain. Coarse **(A)** and fine **(B)** meshes. Enlarged views show the mesh near the wing base. The green region is the faces that the "remote displacement" boundary condition was applied in ANSYS Mechanical to drive the wings. Positional angles **(C,D)**, wingbeat amplitude for downstroke **(E,F)**, and mean positional angle for downstroke **(G,H)**, where blue lines are for wingbase and orange lines are for wingtip. Note the 0 mean positional angle means the wing flaps equal amount for dorsal and ventral directions. In the current case, the mean positional angle tends to be negative, indicating the downward bending. The mean (along each of 2 vein) spanwise strains for coarse and fine meshes **(I)**, where blue and green solid lines are subcosta and radius in fine mesh, respectively, and orange and red dashed lines are subcosta and radius in coarse mesh, respectively. The ensemble average for the mean spanwise strain over nine consecutive wingbeats ($21.75 \leq t/T \leq 30.75$) (J), where blue line is subcosta and orange line is radius. Mean and ±1 SD are shown. The cycle-by-cycle variation in spanwise strain for subcosta **(K)** and radius **(L)**. Cycle 22 corresponds to $21.75 \leq t/T \leq 22.75$, and so on.

Supplemental references

[S1]. Simmons, P. (1977). The neuronal control of dragonfly flight. II. Physiology. J. Exp. Biol. 71, 141–155.

[S2]. Ott, S.R. (2008). Confocal microscopy in large insect brains: Zinc–formaldehyde fixation improves synapsin immunostaining and preservation of morphology in whole-mounts. J. Neurosci. Methods 172, 220–230. 10.1016/j.jneumeth.2008.04.031.

[S3]. Schindelin, J., Arganda-Carreras, I., Frise, E., Kaynig, V., Longair, M., Pietzsch, T., Preibisch, S., Rueden, C., Saalfeld, S., Schmid, B., et al. (2012). Fiji: an open-source platform for biological-image analysis. Nat. Methods 9, 676–682. 10.1038/nmeth.2019.

[S4]. Boyde, A., Mccorkell, F.A., Taylor, G.K., Bomphrey, R.J., and Doube, M. (2014). Iodine vapor staining for atomic number contrast in backscattered electron and X‐ray imaging. Microsc. Res. Tech. 77, 1044–1051. 10.1002/jemt.22435.

[S5]. Jongerius, S.R., and Lentink, D. (2010). Structural Analysis of a Dragonfly Wing. Exp. Mech. 50, 1323–1334. 10.1007/s11340-010-9411-x.